Mapping natural and urban environments using airborne multi-sensor ADS40–MIVIS–LiDAR synergies

Giovanni Forzieri [a,b,*], Luca Tanteri [b], Gabriele Moser [c], Filippo Catani [b]

[a] Climate Risk Management Unit, Institute for Environment and Sustainability, Joint Research Centre, European Commission, Ispra, Italy
[b] Department of Earth Sciences, University of Florence, Italy
[c] Department of Telecommunications, Electronic, and Electrical Engineering, and Naval Architecture, University of Genoa, Italy

ARTICLE INFO

ABSTRACT

The recent and forthcoming availability of high spatial resolution imagery from satellite and airborne sensors offers the possibility to generate an increasing number of remote sensing products and opens new promising opportunities for multi-sensor classification. Data fusion strategies, applied to modern airborne Earth observation systems, including hyperspectral MIVIS, color-infrared ADS40, and LiDAR sensors, are explored in this paper for fine-scale mapping of heterogeneous urban/rural landscapes. An over 1000-element array of supervised classification results is generated by varying the underlying classification algorithm (Maximum Likelihood/Spectral Angle Mapper/Spectral Information Divergence), the remote sensing data stack (different multi-sensor data combination), and the set of hyperspectral channels used for classification (feature selection). The analysis focuses on the identification of the best performing data fusion configuration and investigates sensor-derived marginal improvements. Numerical experiments, performed on a 20-km stretch of the Marecchia River (Italy), allow for a quantification of the synergies of multi-sensor airborne data. The use of Maximum Likelihood and of the feature space including ADS40, LiDAR derived normalized digital surface, texture layers, and 24 MIVIS bands represents the scheme that maximizes the classification accuracy on the test set. The best classification provides high accuracy (92.57% overall accuracy) and demonstrates the potential of the proposed approach to define the optimized data fusion and to capture the high spatial variability of natural and human-dominated environments. Significant inter-class differences in the identification schemes are also found by indicating possible sub-optimal solutions for landscape-driven mapping, such as mixed forest, floodplain, urban, and agricultural zones.

© 2012 Elsevier B.V. All rights reserved.

1. Introduction

Land cover is a crucial variable, which plays an important role in most soil–atmosphere interactions (Feddema et al., 2005). The significance of providing accurate fine-scale land cover maps is emphasized by the evidence of marked impacts of land cover changes on local surface dynamics (Claessens et al., 2009). Remote sensing data classification represents an essential tool for environmental monitoring and sustainable land use management (Melesse et al., 2007), especially in heterogeneous landscapes characterized by many interconnected natural- and human-induced processes (Forzieri and Catani, 2011). Given the large number of diverse land cover types and their possible interclass spectral overlapping, automatic mapping of complex urban/rural patterns represents a

difficult task, particularly when very high spatial resolutions are concerned.

Modern space-borne hyperspectral (e.g., HYPERION, CHRIS/PROBA) and laser scanner (ICESat/GLAS) sensors recently offered an interesting potential in land surface characterization (e.g., Duca and Del Frate, 2008; Goodenough et al., 2003), but may still exhibit possible inaccuracies in monitoring environments that are highly variable in space (e.g., Cavalli et al., 2008; Pignatti et al., 2009). In this context, high-resolution airborne sensors represent enhanced mapping tools (e.g., Gianinetto and Lechi, 2004; Lu et al., 2007; Melgani and Bruzzone, 2004) and also preliminary tests to drive planned satellite-based systems (e.g., PRISMA, EnMAP, HyspIRI, Sentinel). High spatial resolution airborne color-infrared sensors (e.g., Intergraph DMC, ADS40, RC30) provided encouraging classification performances especially in antrophic areas, such as agricultural and urban zones (Belluco et al., 2006; Tansey et al., 2009). Airborne hyperspectral data, such as Multispectral Infrared Visible Imaging Spectrometer (MIVIS), Airborne Visible InfraRed Imaging Spectrometer (AVIRIS), and HyMap, thanks to their high

---

* Corresponding author. Tel.: +39 0332785528; fax: +39 0332786653.
E-mail address: giovanni.forzieri@jrc.ec.europa.eu (G. Forzieri).

spectral resolutions, have demonstrated to be powerful tools to discriminate land cover classes with partially overlapping of spectral signatures in the feature space, such as forest and wetland ecosystems (Colombo et al., 2008; Forzieri et al., in press; Hirano et al., 2003) and geologic features (van Der Meer et al., 2012). Light Detection and Ranging (LiDAR) data have been extensively used for mapping tasks due to their ability to capture the 3D structure of the monitored surfaces, especially in vegetated and built-up areas (e.g., Forzieri et al., 2009; Priestnall et al., 2000).

Several data fusion methods have been successfully tested for classification of different landscape scenarios. Here, we point out that the terms "data fusion" and "multi-source (multi-sensor)" classification are used in this work as synonymous with the meaning of labeling pixels by drawing inferences from several input data sources, according to the definition given by Richards and Jia (2006). A common technique of data fusion for multi-source classification is the stacked vector approach that consists in generating extended pixel vectors stacking together the individual vectors that correspond to each input data source (Richards and Jia, 2006; Tso and Mather, 2000). The fusion of LiDAR and hyperspectral/multispectral data exhibited an interesting potential in several application fields including the retrieval of biophysical and geological properties of land surfaces (Anderson et al., 2008; Forzieri et al., 2012a; Spinetti et al., 2009). The combined use of laser scanner and spectral data was particularly effective in classification tasks to distinguish vegetation types (e.g., Dalponte et al., 2008; Elaksher, 2008; Mundt et al., 2006), anthropogenic surfaces (e.g., Chen et al., 2009), and land cover changes (Forzieri et al., 2012b). Additional derived features, such as texture or DTM-based layers, have been used to improve class discrimination over cropfields and riparian corridors (e.g., Forzieri et al., 2010; Herold et al., 2003).

Mapping approaches based on multisource data can be either contextual or noncontextual depending on the possible use of spatial information. Region- and object-based methods represent a primary subcategory of contextual classification methods. Noncontextual classifiers label the (multi-source) signature of each pixel regardless of all other pixels (e.g., Richards and Jia, 2006), thus discarding the spatial information associated with the image. Contextual approaches use both spectral and spatial information (Moser and Serpico, in press; Moser et al., in press). The former approach bears the obvious advantage of simplicity, but the latter generally includes more powerful classification techniques. Region-based and object-based methods currently play a primary role in the literature of contextual classification, especially when high-resolution data are concerned. A basic region-based approach may be two-step process involving: (1) segmentation of the image into homogeneous regions, possibly representing objects or parts of objects, and (2) classification of those regions (e.g., de Jong and van der Meer, 2004; Navulur, 2007). However, more sophisticated region-based architectures can be devised, depending on the nature of data being analyzed, their spatial resolutions, the computational resource available, and the intended application of the classified data (Lillesand et al., 2008; Moser et al., in press).

Even though the costs of airborne image acquisition are high compared to satellite remote sensing image procurement and may represent an operational constraint in several environmental applications, their exploitation can be viewed both as a preliminary step toward the development of spaceborne advanced monitoring systems and in the perspective of the application to specific monitored areas of particular environmental interest. In light of the recent advances in sensor technology, additional fusion experiments on modern airborne remote sensing data serve for a better understanding of the potential and limitations of current Earth observation systems. In particular, there is a great need for assessing optimized exploitation strategies of multi-sensor remote sensing data to maximize the inter-class separability in

heterogeneous landscape scenarios. In this context, hyperspectral MIVIS, color-infrared ADS40 and LiDAR data represent useful datasets to quantify multi-source synergies for image classification tasks. Given their very high spatial and spectral resolutions, such sensors have separately demonstrated to be effective for detailed land cover mapping (e.g., Belluco et al., 2006; Forzieri et al., in press), but their implementation into data fusion processes is still scarcely explored. For this purpose, in this paper we analyze different fusion strategies involving MIVIS, ADS40, and LiDAR data for classification tasks associated with complex landscapes. We generate an array of standard supervised pixel-based classification scenarios by varying a set of key choices (classifier and remote sensing data combination) and we identify the configuration with the highest accuracy on the test set. Sensor-derived marginal improvements and land cover-based performances are also investigated. The main novel contribution of this paper consists in the experimental investigation of possible synergies among high-dimensional multi-sensor airborne data (MIVIS, ADS40, LiDAR) for the classification of heterogeneous landscapes.

2. Methods

2.1. Study area

The study was conducted over a 20-km stretch of the Marecchia river ($\sim$40 km^2), that sources in Eastern Tuscany and runs at the border of the Emilia-Romagna and Marche regions, in North-Eastern Italy (43°N, 12°E) (Fig. 1). Such study area has been chosen for its complexity in land cover spatial variability and represents an excellent test to quantify multi-sensor remote sensing capability to classify heterogeneous landscapes. The hill slopes are characterized by a significant biodiversity of arboreal species, which include conifer and broad-leaved types, such as oak, pine, cypressus, and spruce (Fig. 1A, mixed forest). Riparian ecosystems exhibit complex patterns with flexible and stiff vegetation in different succession stages, such as willow, arundo donax, heatland, and poplar. Streamside caves for fluvial sediment extraction with related decantation basins are also present in the floodplain (Fig. 1B, floodplain). The valley floor is prevalently made up of fabrics/industrial units (Fig. 1C, urban zones), agricultural fields, such as croplands and olive groves, and semi-natural vegetation, such as meadows (Fig. 1D, agricultural areas).

We defined 17 main target land cover classes to be discriminated: water river (WR), water lagoon (WL), bare soil (BS), asphalt (AS), plowed field (PF), urban fabric (UF), industrial unit (IU), herbaceous (HE), heatland (HL), arundo donax (AD), poplar (PL), oak (OK), pine (PN), cypressus (CY), spruce (SP), willow (WI), and olive (OV).

2.2. Remote sensing and field data

For this study we used multi-sensor data, including optical ADS40, hyperspectral MIVIS, and LiDAR. Color-infrared aerial digital image data acquired by ADS40 have 4 spectral bands: blue (0.430–0.490 μm), green (0.535–0.585 μm), red (0.610–0.660 μm), and near-infrared (NIR; 0.835–0.885 μm). The data have 12-bit radiometric depth and 0.2-m pixel size. MIVIS is a whiskbroom hyperspectral sensor with high spatial (3-m pixel size) and radiometric (12 bit) resolution, and with variable spectral resolution (sr) depending on the spectrometer. This sensor records 102 bands spanning across the visible (20 bands within the 0.43–0.83 μm range with $sr = 0.02$ μm), near-infrared (8 bands within the 1.15–1.55 μm range with $sr = 0.05$ μm), middle-infrared (64 bands within the 1.983–2.478 μm range with $sr = 0.009$ μm) and thermal-infrared (10 bands within the 8.18–12.7 μm range
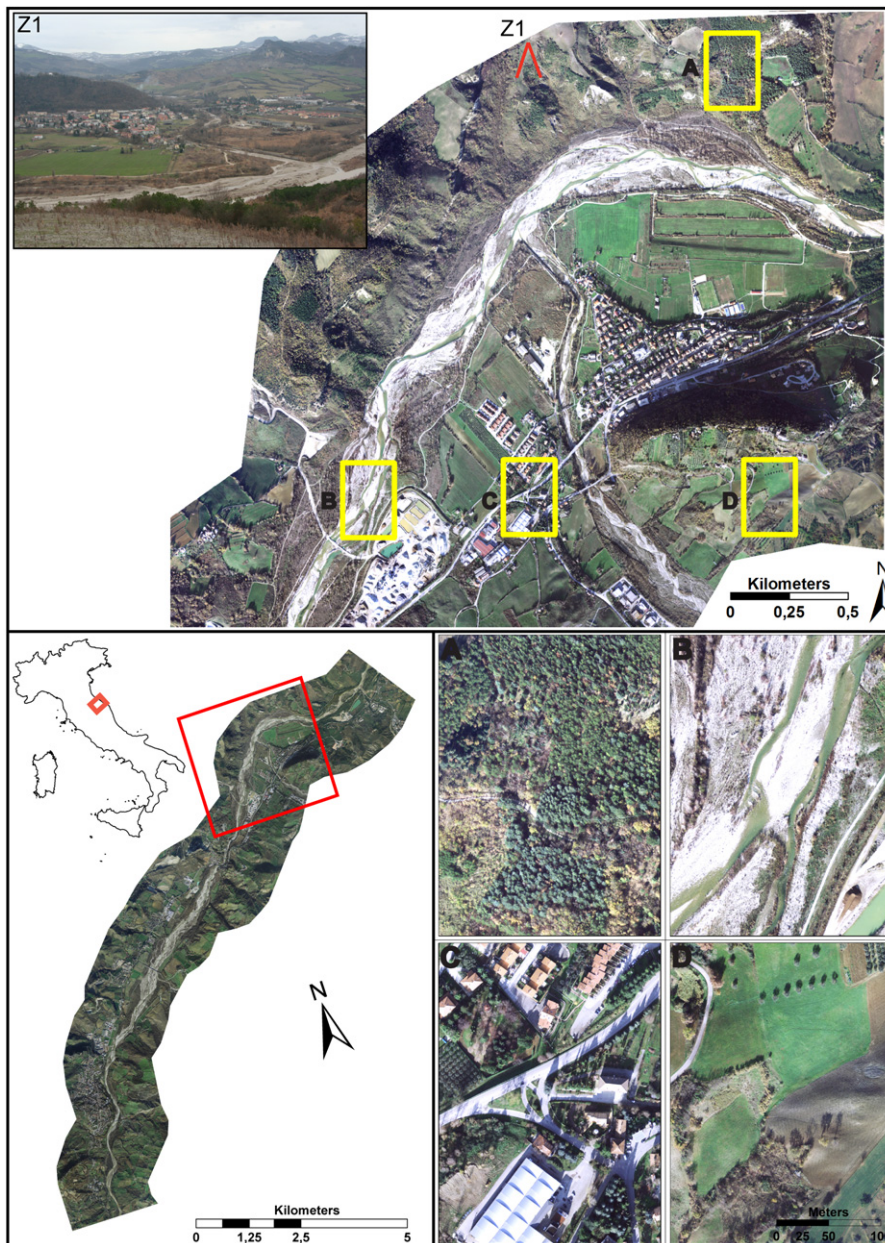
Fig. 1. Study area: key map and entire monitored 20-km stretch of the Marecchia river (Emilia Romagna, Italy) (bottom left map), reference 3-km × 3-km inset box and panoramic view (Z1) (upper map), typical investigated landscapes including mixed forest (A), floodplain (B), urban zone (C) and agricultural area (D).

with sr from 0.34 to 0.54 μm). LiDAR data were provided in terms of Digital Terrain Model (DTM) and Digital Surface Model (DSM) with 1-m spatial resolution and 0.2-m vertical accuracy. The airborne platform (Casa 212/C I-MAFE) was prepared for two camera hatches. Multi-sensor data were acquired in December 6 and 11, 2009, within a time-frame spanning from 10.00 to 14.00 UTC: ADS40 and MIVIS data were simultaneously acquired in the former acquisition date, while LiDAR data were taken in the latter date.

Training and test pixels have been collected during the same season of the remote sensing acquisitions through field surveys and through the visual interpretation of the ADS40 image. While delineating training and test polygons, pixels located along the edges between land cover types were avoided to reduce the impact of potential small registration errors and to prevent the inclusion of mixed pixels in the training and test sets. The resulting sample sizes are listed in Table 1 in terms of number of 1-m pixels.

2.3. Methodology

The proposed procedure explores different strategies of exploitation of multi-sensor remote sensing data for fine-scale mapping of 17 land cover classes. The method generates a large array of classification scenarios obtained with different sensor/setting combinations and, similar to a model identification problem, identifies the combination which maximizes the classification accuracy. The configuration to identify include: (1) classification algorithm (al); (2) multi-source data combination (FS); and (3) number n of hyperspectral channels. The array of the classification maps can be described by the following mathematical notation:

$$H = \mathrm{K}(al, FS, n) \tag{1}$$

where H is the classification accuracy associated with the triplet (al, FS, n) used as input in the classification routine (K).

Table 1
The seventeen spectral classes used for training and testing, their codes, and the corresponding number of 1-m pixels.

Land cover class	Code	Training set [# 1-m pixels]	Testing set [# 1-m pixels]
Water river	WR	23,855	26,368
Water lagoon	WL	4448	3310
Bare soil	BS	52,414	55,022
Asphalt	AS	14,253	10,855
Plowed field	PF	90,262	81,411
Urban fabric	UF	16,557	14,587
Industrial unit	IU	13,748	12,515
Herbaceous	HE	300,477	265,074
Heatland	HL	56,977	50,986
Arundo donax	AD	10,258	9828
Poplar	PL	13,114	13,358
Oak	OK	96,804	97,532
Pine	PN	15,793	15,718
Cypressus	CY	11,241	11,996
Spruce	SP	26,774	29,576
Willow	WI	6446	6490
Olive	OV	5976	5116

2.3.1. Explored classification solutions

Fig. 2 displays the flowchart of the generation of the explored array of classification results. This generation is organized in five sequential steps.

2.3.1.1. Pre-processing.
The remote sensing data were orthorectified and co-registered in the UTM-WGS84 projection by ground control points. MIVIS radiance data were used for classification, i.e., no preliminary atmospheric correction was applied to map radiance to reflectance data. On one hand, this correction would allow atmospheric effects affecting spectra absorption features (e.g., effects associated with the bidirectional reflectance distribution function, adjacency effects) to be addressed. On the other hand, atmospheric correction in itself may introduce biases or distortions, which might negatively affect the classification performances. Therefore, similar to many previous applications of supervised classification to the problem of land-cover mapping from hyperspectral sensors (e.g., Landgrebe, 2003; Serpico and Moser, 2007), data were used in radiance format for the classification study discussed here.

Fig. 2. Flowchart of the developed classification scheme. Data, pre-processing, feature extraction, feature reduction, stacked vector and mapping procedures are differently displayed according to the reference shaded color.

2.3.1.2. Feature extraction.
To better discriminate the spectral signatures of the shadow and shadow-free areas we calculated the hillshade modeling (HM) by using the Digital Terrain Model and the solar position parameters related to the spectral data acquisition time (Burrough and McDonell, 1998). We also calculated the normalized Digital Surface Model (nDSM) by the simple subtraction of DTM and DSM to increase the inter-class separability for the 3D-derived information. Finally we computed three popular texture features (range, mean, variance, collectively labeled in the following as TX) estimated by means of a first-order statistical analysis (Haralick et al., 1973) with a 3 m × 3 m window size on a simulated panchromatic channel. This channel is defined as the average of the ADS40 channels weighed on the spectral acquisition range of each band (Wang et al., 2010). A preliminary analysis supported the suitability of the selected window size to capture spatial correlation patterns (e.g., croplands, olive fields, and road networks). Hillshade modeling (HM), normalized digital surface model (nDSM) and texture layers (TX) have been used in this study as additional features in the mapping procedure.

2.3.1.3. Feature reduction.
Within the available MIVIS dataset, we have only used the first 24 bands (spanning within the 0.43–1.319 μm spectral range), as the remaining channels were corrupted (Forzieri et al., in press). The main problematic issue in the analysis of hyperspectral data is related to the high dimensionality of the spectral space: when increasing the number of features, the Hughes' phenomenon (Hughes, 1968) may occur, that consists in a loss of classification accuracy caused by the mismatch between the number of available training samples and the number of samples that should be needed to reliably estimate the classifier parameters (Landgrebe, 2003). In order to reduce possible hyperspectral-derived dimensionality effects, we applied the Sequential Forward Selection (SFS) to the MIVIS bands (Serpico et al., 2002). This selection algorithm is based on a sub-optimal iterative search strategy, it is initialized with an empty set of selected features, and iteratively identifies the best feature subset (see Fig. 2) that can be obtained by adding to the current feature subset one feature at a time (whose size ranges in our case from 1 to 24) until the desired number n of features is achieved. The Jeffries–Matusita measure was used as an inter-class distance measure to guide this selection process (Richards and Jia, 2006). We used feature selection strategies instead of feature space transformations to preserve the physical meanings of the discriminant components of the MIVIS subsets. Within the selection methods, we chose SFS thanks to its limited computational burden and because it has been demonstrated to be a powerful and efficient tool in hyperdimensional feature space reduction (Serpico et al., 2002).

2.3.1.4. Stacked vector approach.
A straightforward approach to classify mixed data is to form extended pixel vectors stacking together the individual vectors that correspond to each input data source (stacked vector method; Richards and Jia, 2006; Tso and Mather, 2000). Here, 16 options for stacking the original (ADS40, MIVIS) and derived information (nDSM, HM, TX) were explored. The data from the resulting 16 multi-source feature spaces (FS, in Fig. 2) – which differently combine the available remote sensing information (Table 2) – were resampled at the common 1-m spatial resolution. The resampling cell size was chosen to finely capture the spatial variability of land covers without asking for massive computing power or excessive computing time.

2.3.1.5. Mapping procedure.
The generated multi-stacks were classified by means of three popular classifiers (al in Fig. 2) that have been chosen in this study for their simple implementations and computational efficiencies: the well known Maximum Likelihood (ML, Richards and Jia, 2006), Spectral Angle Mapper (SAM, Kruse
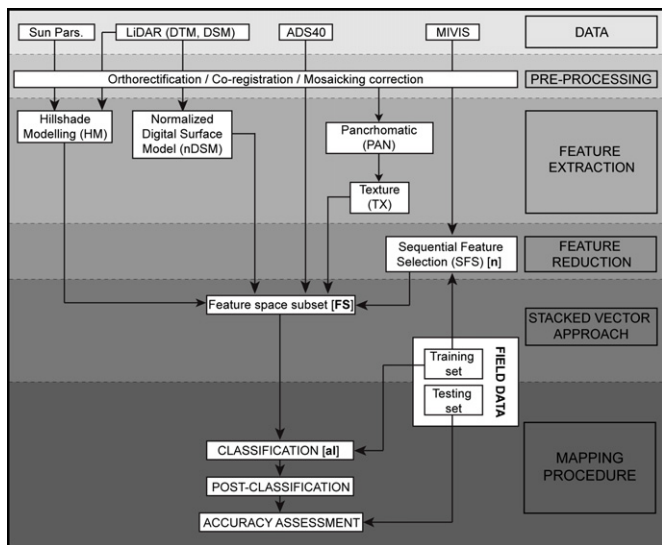
Table 2
The sixteen feature spaces used in the classification procedure (FS1, ..., FS16) including: normalized Digital Surface Model (nDSM), hillshade modeling (HM), multispectral data (ADS40), texture layers (TX) and hyperspectral data (MIVIS). Admissible numbers of input features are shown in brackets.

Feature space	nDSM [1]	HM [1]	ADS40 [4]	TX [3]	MIVIS [1:24]
FS1			X		
FS2					X
FS3	X		X		
FS4	X				X
FS5	X		X		X
FS6		X	X		
FS7		X			X
FS8	X	X	X		
FS9	X	X			X
FS10	X	X	X		X
FS11			X	X	
FS12				X	X
FS13	X		X	X	
FS14	X			X	X
FS15	X		X	X	X
FS16	X	X	X	X	X

et al., 1993), and Spectral Information Divergence (SID, Chang, 2000) classifiers. Since SAM needs as input, at least, a two-band set, all classification scenarios were accordingly developed with a minimum of two input bands to better compare the performances of different algorithms. In order to reduce possible salt-and-pepper effects, we also applied a post-classification majority filter to the resulting maps with a 3 m × 3 m kernel size (Yuan et al., 2005).

This strategy produced 1104 land cover maps with different configurations of the afore-mentioned variables (3 classifiers × 16 feature spaces × 23 hyperspectral subsets).

2.3.2. Classification accuracy assessment

Training/testing samples were used to calibrate/validate each generated configuration. The classification performances were quantified in terms of confusion matrix (M), overall accuracy (OA), commission (COM)/omission (OMI) errors and kappa conditional statistics (K_s).

Marginal improvements derived from each individual data source were also investigated by extracting, from the full array, the subsets that include/exclude the source under investigation. For each data source, we selected two different subsets (X, Y) defined as follows:

$$X = K(al, FS = fs_x, n),$$
$$Y = K(al, FS = fs_y, n), \quad al = ML, SAM, SID; \quad n = 2, \ldots, 24 \quad (3)$$

where fs_x (fs_y) denote the feature spaces that include (exclude) the considered source. These spaces are listed in Table 3 with regard to each source (ADS40, MIVIS, nDSM, HM, and TX). Then, the Behrens–Fisher statistics with 0.95 confidence level was computed for testing the difference between the means (μ) of the two overall accuracies calculated separately with the X and Y subsets. We analyzed two different tests:

$$t_1 : \begin{cases} H_0 : \mu_x = \mu_y \\ H_1 : \mu_x > \mu_y \end{cases}; \qquad t_2 : \begin{cases} H_0 : \mu_x = \mu_y \\ H_1 : \mu_x < \mu_y \end{cases} \quad (4)$$

The rejection of the null hypothesis H_0, in favor of the target hypothesis H_1, in the t_1 (t_2) case indicates a prevalent positive (negative) impact of the investigated data source on the classification performances. The large size of the classification array (1104 land cover maps) allowed for a robust quantification of the statistical significance of the possible benefits associated with each source (Kottegoda and Rosso, 1997).

2.3.3. Classification scheme identification

As mentioned previously, the behavior of the classification performances within the array of generated classification results can be assimilated to a three-parameter function ($H = K(al, FS, n)$), whose global maximum value identifies the optimal classification scheme, with respect to the criterion of maximizing the overall classification accuracy on the test set. In order to highlight specific parameter-dependent improvements and to define possible sub-optimal alternatives we described the classification scheme identification through 3 sequential steps, by progressively fixing one optimal configuration variable at a time and by accordingly reducing the size of the search space:

1st-step array subset, classifier choice;

$$H_{al}(FS, n) = \max_{al}[K(al, FS, n)] \quad (5)$$

2nd-step array subset, choice of the stacked vector configuration;

$$H_{al,FS}(n) = \max_{(FS)}[H_{al}(FS, n)], \quad (6)$$

3rd-step array subset, choice of the number of hyperspectral channels.

$$H_{al,FS,n} = \max_{(n)}[H_{al,FS}(n)], \quad (7)$$

We also explored the variability of the three key parameters (al, FS, n) across the investigated land covers to assess possible sub-optimal classification solutions more suited to specific environments, such as mixed forest, floodplain, urban, and agricultural zones.

3. Results and discussions

3.1. Classification algorithm performances (al identification)

In this section we focus on the impact of the tested classifiers (ML, SAM, SID) on the overall accuracy to identify the best performing classification algorithm (first step of the identification scheme). Fig. 3 is organized in 16 plots, each related to an individual investigated feature space (FS variable). The selected subsets composed of increasing numbers of MIVIS bands (n variable) and overall accuracies (OA) are displayed on the x-axis and y-axis, respectively (see Section 3.3 for details on the optimization of n). The three different color lines refer to the three classifiers.

Classification accuracies are obviously n-independent in the feature spaces not including MIVIS bands (Fig. 3A, C, F, H, M and O). It is evident that ML provides higher performances with all the 16 feature space configurations, especially in the highest-dimensional cases (Fig. 3B–E, G, I, L, N and P–R), than SAM and SID. These two classifiers generally exhibit comparable accuracies, with slightly better performances of SAM than of SID in low-dimensional feature spaces (Fig. 3A, C, F, H and M) and vice versa in high-dimensional ones (Fig. 3E, L, N and P). The improved accuracy of ML over SAM and SID is an expected result due to the capability of ML to take into account first- and second-order statistics of the data associated with each class. On the contrary, SAM and SID essentially characterize each class with a unique prototype and consequently do not allow appreciating the shapes of the class-conditional distributions in the feature space (Richards and Jia, 2006).

ML is based on a Gaussian unimodal model for each class-conditional statistics. In order to verify the possible unimodal spectral distribution of the data associated with each land cover, we applied the Hartigan test (Hartigan and Hartigan, 1985) and

Table 3

Array subsets for each input source (ADS40, MIVIS, nDSM, HM, TX) used in the source marginal improvement assessment: fs_x and fs_y include and exclude the reference data source, respectively. Statistical test results (t_1 and t_2) of the array subsets for each input source are listed: 1 (0) values of the Behrens–Fisher test indicate rejection (no rejection) of the H_0 null hypothesis with 0.95 confidence level.

Tested features	Array subset		Behrens–Fisher test	
	fs_x	fs_y	t_1 $H_0: \mu_x = \mu_y H_1: \mu_x > \mu_y$	t_2 $H_0: \mu_x = \mu_y H_1: \mu_x < \mu_y$
ADS40	1,3,5,6,8,10,11,13,15,16	2,4,7,9,12,14	0	1
MIVIS	2,4,5,7,9,10,12,14,15,16	1,3,6,8,11,13	1	0
nDSM	3,4,5,8,9,13,14,15,16	1,2,6,7,11,12	1	0
HM	6,7,8,9,10,16	1,2,3,4,5,11,12,13,14,15	0	0
TX	11,12,13,14,15,16	1,2,3,4,5,6,7,8,9,10	1	0

estimated the corresponding probability through a 500-sample bootstrap permutation scheme. High probability values of the uni-modal distribution hypothesis are obtained for normalized digital surface and texture features and for most MIVIS bands, especially when conditioned to forest classes (average probability > 0.75), thus supporting the use of ML for classification purposes in the considered case study. More sophisticated approaches, based for example on classifier Ensembles, Markov random fields or support vector machines, could represent valuable alternatives to further improve the classification accuracy (e.g., Melgani and Bruzzone, 2004; Moser and Serpico, in press; Pal and Mather, 2005; Zhang et al., 2011).

3.2. Feature space combination (FS identification)

To optimally combine the available multi-source remote sensing data, the feature space configuration (FS) corresponding to the highest accuracy was determined (second step of the identification scheme). To this purpose, a preliminary testing analysis was performed to assess the marginal improvements derivable from each data source. Fig. 4 shows 5 plots related to the marginal improvements of ADS40, MIVIS, nDSM, HM, and TX. Each plot displays the distributions of overall accuracies (OA, on the y-axis) of the two reference array subsets (X and Y, on x-axis), defined in Eq. (3) and listed in Table 4. The classification performances are displayed through box plots where the central mark is the median (Me), the edges of the box are the 25th and 75th percentiles, and the whiskers extend to the most extreme data points. X median values greater (lower) than Y median values suggest possible source-dependent positive (negative) impacts.

Results suggest that the use of ADS40 in the classification process mainly negatively affects classification performances (Me(X) < Me(Y)) in Fig. 4A and t_1 = 0 and t_2 = 1 in Table 3). This negative effect is likely imputable to the possible redundancy due to the overlapping of spectral signatures between ADS40 and MIVIS in the visible range. Furthermore lower probability values in the Hartigan test for unimodal distribution were also found for the ADS40 channels. This last issue could highlight possible limitations of the
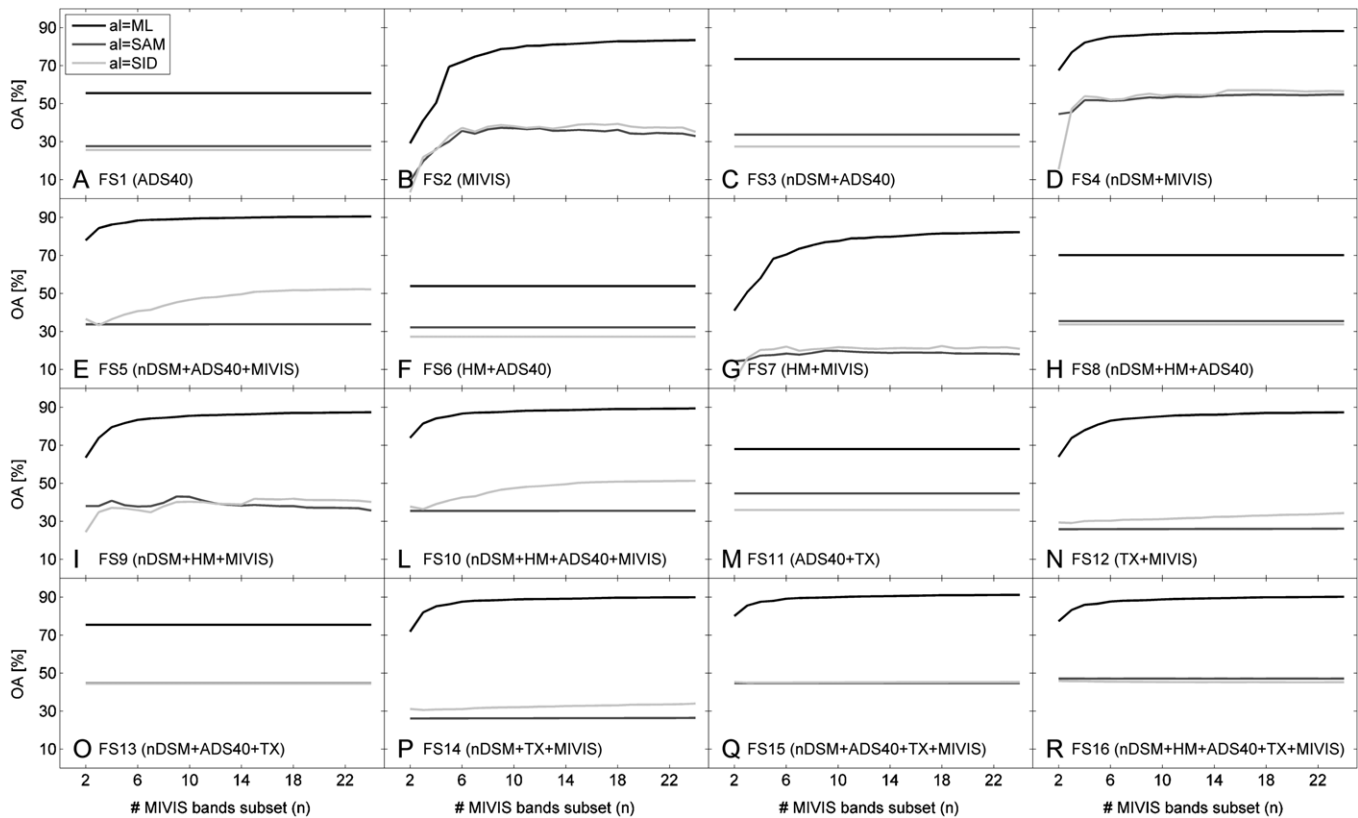

Fig. 3. Classification accuracies for the sixteen tested feature spaces displayed separately on different plots. Selected subsets of increasing input MIVIS bands and overall accuracies (OA) are displayed on the x-axis and y-axis, respectively. The three different color lines refer to the three classification algorithm performances (ML, SAM, SID), as indicated in the legend.
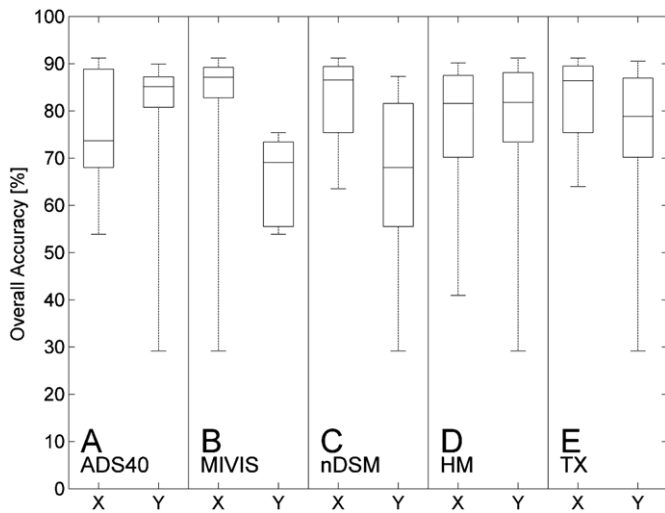
Fig. 4. Marginal improvements of specific data source: ADS40 (A), MIVIS (B), nDSM (C), HM(D) and TX(E). Each plot displays the distributions of overall accuracies (OA, y-axis) of the two reference array subsets (X and Y, x-axis, see Table 3 for the definition). The classification performances are displayed in box plots where the central mark is the median and the edges of the box are the 25th and 75th percentiles, the whiskers extend to the most extreme data points.
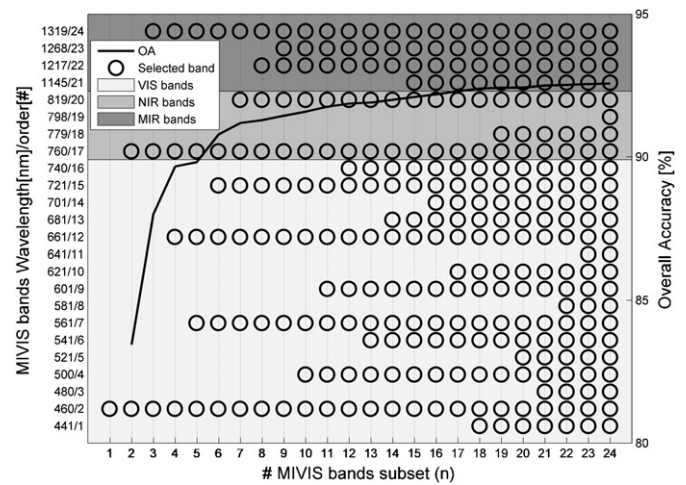

Fig. 5. The iterative selection of MIVIS subsets (on x-axis) with the progressive increasing of the number of hyperspectral bands (on left y-axis). Selected bands are displayed in black circles, while gray shaded colors define the reference spectral regions: visible (VIS), near infrared (NIR) and middle infrared (MIR). The overlaid overall accuracy is visualized as a solid black line and refers to the right y-axis.

selected classifiers, which essentially assume a monomodal behavior for each class-conditional statistics, in correctly capturing the spectral signature of this sensor.

Hillshade modeling (HM) does not improve the mapping accuracy (Me(X)∼Me(Y) in Fig. 4D and $t_1 = 0$ and $t_2 = 0$ in Table 3). Although HM well discriminates shaded/free-shaded areas in urban zones, this marginal classification benefit is negatively counterbalanced by the HM-derived noise in forest patterns (not shown here for brevity).

In contrast, MIVIS, nDSM, and TX features represent the most important discriminant contributions in the classification process (Me(X) > Me(Y) in Fig. 4B, C and E and $t_1 = 1$ and $t_2 = 0$ in Table 3). Despite the evident cutoff of the original MIVIS bands (from 102 to 24 bands) results confirm the high capability of the remaining hyperspectral channels of classifying complex landscapes. Furthermore, LiDAR-derived 3D information (nDSM) and spatial textural features (TX) introduce additional discriminant information and positively contribute to maximize the inter-class separability.

Table 4 lists, for each explored feature space combination, the maximum classification accuracy, the ranking (r_k), and the

Table 4

Maximum overall accuracy (MOA), corresponding ranking order (r_k) and relative improvement with respect to FS1 (I_{FS1}) and FS2 (I_{FS2}), for each feature space (FS1,..., FS16). Relative improvements are calculated as $I_{FSi}(FSj) = 100 \cdot [MOA(FSj) - MOA(FSi)]/MOA(FSj)$ where $i = 1, 2$ and $j = 1, ..., 16$.

Feature space	MOA (%)	Rank r_k	I_{FS1} (%)	I_{FS2} (%)
FS1	55.51	15	0.00	−50.24
FS2	83.4	9	33.44	0.00
FS3	73.42	12	24.39	−13.59
FS4	88.21	6	37.07	5.45
FS5	90.54	2	38.69	7.89
FS6	53.9	16	−2.99	−54.73
FS7	82.25	10	32.51	−1.40
FS8	70.2	13	20.93	−18.80
FS9	87.39	7	36.48	4.57
FS10	89.38	5	37.89	6.69
FS11	68	14	18.37	−22.65
FS12	87.32	8	36.43	4.49
FS13	75.41	11	26.39	−10.60
FS14	89.91	4	38.26	7.24
FS15	91.19	1	39.13	8.54
FS16	90.17	3	38.44	7.51

relative improvements as compared to the original sets of ADS40 (FS1) and MIVIS (FS2) channels. The use of multi-source data leads to classification improvements ranging up to ∼40% and ∼8% as compared to ADS40 and MIVIS alone. Interestingly, FS15 (ADS40 + MIVIS + TX + nDSM) represents the optimal multi-source configuration (OA = 91.19%, Table 4). This identified best combination represents an extreme point of the box plot in Fig. 4A (percentile > 75th). Comparable performances are obtained on configurations without ADS40 (e.g., FS14, OA = 89.91%, Table 4). Although, as discussed above, ADS40 generally yields a negative impact on the classification performances, as demonstrated through t-tests, its use can lead to improved accuracy if included within specific classification schemes. This might be interpreted as due to the 0.835–0.885 μm spectral range covered by ADS40 but not by MIVIS.

In the following sections FS15 (ADS40 + MIVIS + TX + nDSM) is retained as the best configuration of multi-source data for classification of heterogeneous landscapes on the considered data set.

3.3. Hyper-spectral contribution (n identification)

The number n of MIVIS channels remains the last issue (third step of the identification scheme) to determine in the proposed multi-source data fusion scheme. Fig. 5 shows the iteratively selected MIVIS subsets based on the SFS (x-axis) and the available hyperspectral bands (left y-axis) included in FS15. The selected bands are displayed in circles, while gray shaded colors define the reference spectral regions: visible (VIS), near infrared (NIR), and middle infrared (MIR). The overlaid overall accuracy (OA) is visualized as a solid black line and refers to the right y-axis.

The MIVIS bands are iteratively selected from the VIS, NIR, and MIR ranges, thus suggesting that the whole spectral span of the sensor is relevant for class discrimination, at least, for the considered data set. This result can be related to the high number and spatial variability of complex landscapes that likely benefit from spectral contributions from all the investigated spectral regions. The OA curve shows a sharp increment up to the #6 MIVIS bands subset and a subsequent monotonically increasing trend. This behavior suggests that the data variability may be prevalently captured by the 6-feature subset (#2, 7, 12, 15, 17, 24 MIVIS bands), at least, with respect to the task of discriminating the considered land cover classes. The highest accuracy (OA = 91.19%) is obtained with all
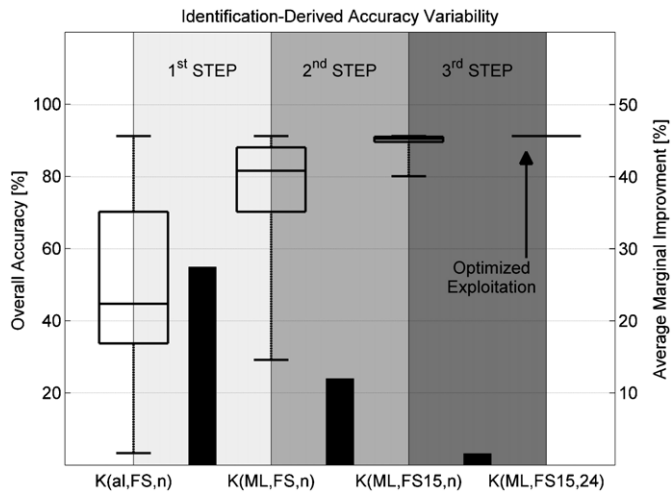
Fig. 6. Synoptic view of the accuracy improvements resulting through the three steps of the procedure adopted to identify the optimal classification scheme K(ML,FS15,24). Each box plot displays the variability of the overall accuracies of the mentioned array subsets: the central mark is the median, the edges of the box are the 25th and 75th percentiles, the whiskers extend to the most extreme data points. Black bars indicate the average marginal improvement (AMI) obtained by the identification process (in shaded colors) by referring to the right *y*-axis.

MIVIS channels and is used as a reference hyperspectral configuration for the final optimized exploitation.

3.4. Marginal accuracy improvements

Fig. 6 shows a synoptic view of the accuracy improvements resulting from the adopted classification scheme as compared to the original full array, K(*al*,*FS*,*n*) up to the final solution, K(ML,FS15,24), identified through the aforementioned 3-steps (in different gray scales). Each box plot displays the variability of the overall accuracies of the reference array subset labeled on the *x*-axis: the central mark is the median, the edges of the box are the 25th and 75th percentiles, the whiskers extend to the most extreme data points, whose range is indicated as DR (data range) in the following lines. Black bars indicate the average marginal improvement (AMI) associated with each step and obtained as the difference between the average values of the classification accuracies in two subsequent array subsets.

The first two identification steps (i.e., those related to the *al* and *FS* variables) prove most effective in reducing classification errors. The classifier selection (K(*al*,*FS*,*n*) → K(ML,FS,*n*)) significantly lowered the variability in classification accuracy (DR from ∼90% to ∼60% with AMI ∼28%). The subsequent selection of the feature-space configuration provides for a further reduction in the range of accuracies (DR from ∼60% to ∼10%) and for an enhancement in classification performance (AMI ∼ 12%), (K(ML,FS,*n*) → K(ML,FS15,*n*)). Although the third step – the optimization of *n* (K(ML,FS15,*n*) → K(ML,FS15,24)) – has a smaller impact on the final classification accuracy than the previous steps (DR decreased from ∼10% to 1%, AMI = ∼2%), it allows for an important accuracy improvement for certain classes, i.e., water bodies (WR, WL, reduction of commission/omission errors of ∼50–70%), forest plant species (OK, PN, CY, SP, reduction of commission/omission errors of ∼50%) and agriculture zones (PF, HE, reduction of commission/omission errors of ∼70–80%).

3.5. Optimized multi-sensor data fusion

The resulting scheme, characterized by the ML classifier and by the feature space including ADS40, TX, nDSM, and the full set of

MIVIS bands, is retained as the best performing multisource classification configuration with respect to the discrimination of the 17 classes in the considered data set. The final majority filter allows reaching a 92.57% OA. Fig. 7 shows the obtained high resolution land cover map: the entire monitored transect (bottom left map); the 3-km × 3-km reference window (upper map); and four zoomed classification views on typical landscapes (inset boxes A, B, C, and D). It is evident by a visual comparison of Figs. 1 and 7 that the obtained classification map captures well the spatial variability of the monitored area, especially considering that, at the data acquisition times, most of the vegetation types were in the senescence phase and consequently exhibited low reflectance values.

The coverage data, which exhibit the lowest error rate, are – as expected – the classes with well defined spectral signatures such as water river (COM(WR) = 1.38%, OMI(WR) = 3.66%), bare surfaces (COM(BS) = 3.58%, OMI(BS) = 5.92%), plowed fields (COM(PF) = 1.84%, OMI(PF) = 2.48%), herbaceous patterns (COM(HE) = 0.97%, OMI(HE) = 2.32%), and oak forests (COM(OK) = 3.08%, OMI(OK) = 14.71%). However, by referring to the confusion matrix M (M(*u*,*v*)) expressed in terms of percentage values (where the (*u*, *v*)-th entry M(*u*, *v*) refers to pixels classified in land cover *u* and belonging to the test set of land cover *v*), persistent errors are found due to possible inter-class spectral overlapping: bare surfaces classified as asphalt (M(AS, BS) = 11.78%); some industrial units labeled as urban fabric (M(UF,IU) = 21.33%); heatlands, herbaceous, oak, poplar and arundo donax partially incorrectly detected (e.g., M(HL,HE) = 5.33%, M(HL,OK) = 5.97%, M(AD,HL) = 9.96%, M(AD,OK) = 14.36%, M(PP,OK) = 37.01%); misclassifications in mixed conifer forests (M(CY,SP) = 26.47%, M(PN,SP) = 5.39%); possible errors between willows and poplar (M(WI,PP) = 10.13%), and misclassification errors on olive groves and herbaceous fields (M(OV,HE) = 24.12%).

3.6. Possible land cover-based optimized solutions

The optimized classification scheme represents the configuration that best performs on the considered 17-class set of land covers. Exploring the possible dependences of the aforementioned identification process on land cover can suggest possible alternative strategies to extend the proposed approach to landscapes with only certain land covers or with a marked predominance.

Fig. 8 shows the key variables for each land cover and for the top 10 classification schemes: the *al*, *FS*, and *n* choices that maximized the kappa conditional statistics are displayed in plots A–C. Rank order and land covers are shown on the *x*-axis and *y*-axis, respectively. For the sake of clarity, we grouped the land cover classes as: mixed forest (OK, PN, CY, SP); floodplain (WR, WL, RS, HL, AD, PL, WI); urban zone (AS, UF, IU); and agricultural area (PF, HE, OV).

3.6.1. Mixed forest

ML represents the best candidate classifier for all the monitored vegetation species (Fig. 8A) and is supported by significant probabilities of unimodal distributions in the Hartigan tests. Oak (OK), pine (PN), and cypressus (C) are better identified through FS7, FS5, FS4, respectively, as the preferential multi-source combinations maximizing the kappa conditional statistics (Fig. 8B), thus confirming the central role of hyperspectral data for classification of complex forest landscapes. The selected MIVIS subset is generally large (about > 16 channels, Fig. 8C). Interestingly, spruce patterns (SP) show multiple sub-optimal solutions in terms of *FS* and *n*.

3.6.2. Floodplain

ML represents the best classifier within the considered ones, for all the land covers with the exception of water lagoon (WL) where SID performs better in terms of kappa conditional statistics (Fig. 8A). Feature space combinations very different from the
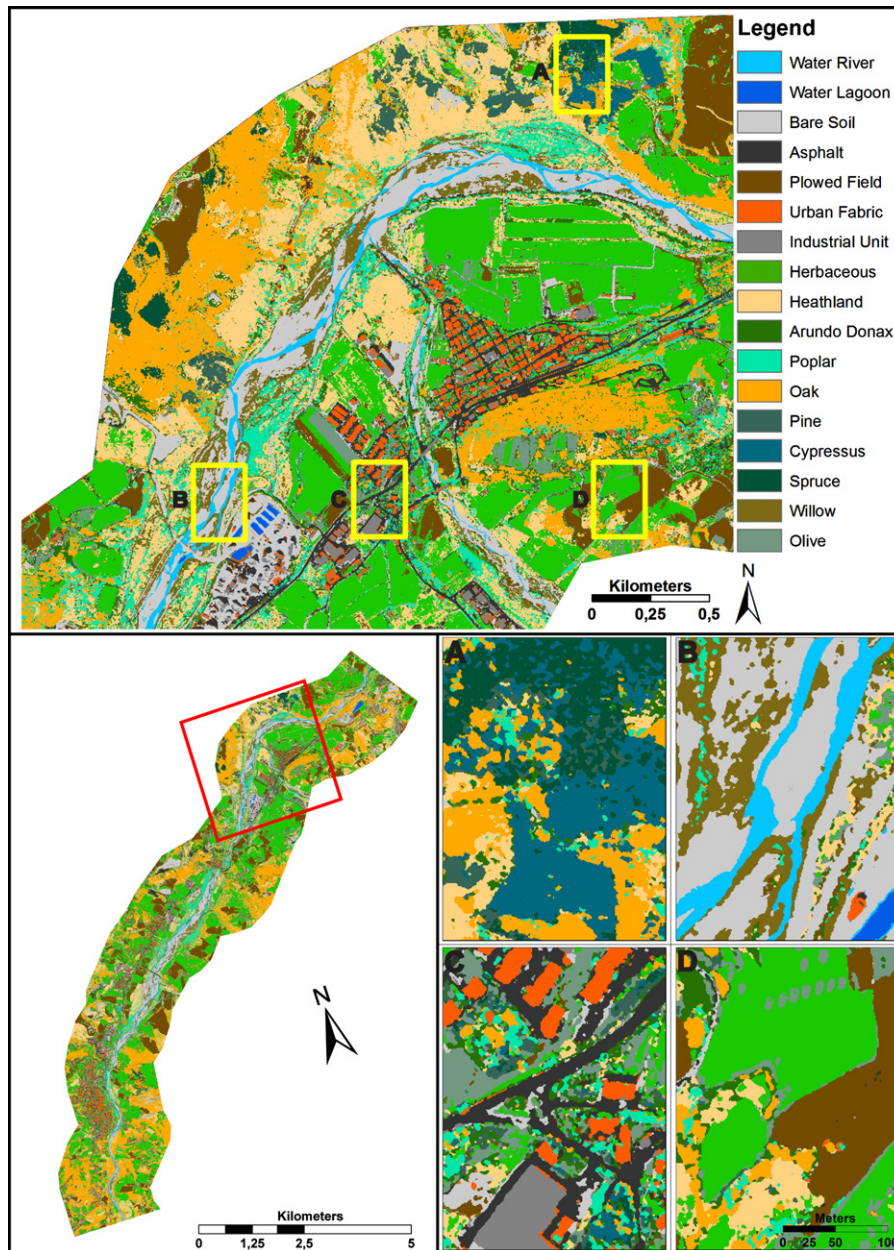
Fig. 7. Classification map resulting from the proposed optimized exploitation of multi-source remote sensing data, K(ML,FS15,24). Entire monitored 20-km stretch (bottom left map), reference 3-km × 3-km inset box (upper map), typical investigated landscapes including mixed forest (A), floodplain (B), urban zone (C) and agricultural area (D).
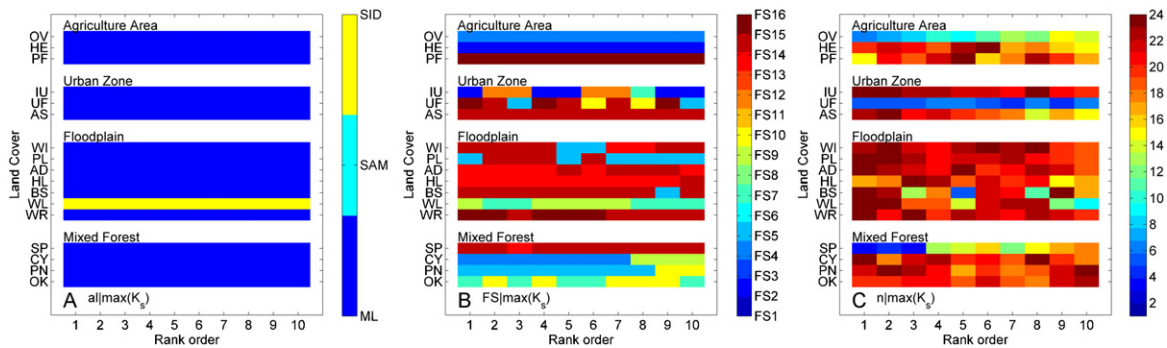

Fig. 8. Main classification variables for 4 grouped typical landscapes: mixed forest, floodplain, urban zone and agricultural area. Algorithm (al), feature space (FS) and MIVIS subset (n) maximizing kappa conditional statistics (K_s) are shown on plots A/B/C for each land cover and for the top 10 classification schemes. Rank order and land cover are shown on the x-axis and y-axis, respectively.

reference optimized solution K(ML,FS15,24) are identified for WL (FS7–9). Possible multi-modal spectral distributions of the surface response (low probability of unimodal distribution), possibly impacting on the performances of ML, are found through the Hartigan test (p(WL) = 0.05) and could be imputable to a high spatial variability of suspended sediments into the monitored lagoons. Analogously to forest landscapes, the best multi-source combinations for the riparian vegetation prevalently include MIVIS-based schemes (such as FS14, FS15 and FS16 for AD, WR, HE, HL, AD, PL, Fig. 8B). A certain agreement is reached, with the identification of a MIVIS subset, between land covers of typical floodplain areas and the optimized solution (n > 20) (Fig. 8C).

3.6.3. Urban zone

Within the considered classifiers, ML represents the best candidate for the monitored land cover classes in urban scenarios, such as asphalt (AS), urban fabric (UF) and industrial unit (IU). MIVIS, normalized Digital Surface Model, texture, and hillshade modeling play the most important contribution and are then selected into the multisource combination FS2, FS15, FS16 (Fig. 8B). Lower dimensionality MIVIS subsets are preferred (n < 7) for urban fabric over industrial unit and asphalt (n > 16) (Fig. 8C).

3.6.4. Agricultural area

Herbaceous (HE) and plowed fields (PF) are well discriminated by ML according to the reference optimized solution (Fig. 8A). For HE and OV, preferential feature space combinations are represented by FS2 and FS4. FS16, by exhibiting a positive contribution of texture layers, is selected as the best feature space for plowed field. Mainly lower dimensional MIVIS subsets (n < 20) than in K(ML,FS15,24) and multiple valuable alternatives with different hyperspectral bands are found appropriate for agricultural land covers.

4. Conclusions

In this paper we investigated an optimized scheme to jointly exploit hyperspectral MIVIS, color-infrared ADS40, and LiDAR data for land cover mapping of heterogeneous landscapes. The methodology focuses on the generation of an array of possible classification scenarios obtained by varying classifiers, multi-source stacks, and subsets of hyperspectral channels, and on the subsequent identification of the best performing configuration.

The proposed procedure resulted a valuable tool for identifying the optimal multi-source remote sensing data combination (with respect to the criterion of classification performances over test samples) by providing a final accurate map (OA = 92.57%). Among the three tested classifiers (ML, SAM, SID), the Maximum Likelihood is confirmed to be a suitable algorithm for mapping purposes (classifier selection has a 28% impact on the final optimized exploitation OA). The feature space including ADS40 (only in certain data combinations), nDSM, TX, and MIVIS data was the optimal multisource dataset to maximize class discrimination (additional 10% on the final OA). In particular, the optimal hyperspectral subset turned out to be the full available set of MIVIS channels (2% further marginal improvement). Significant inter-class differences are also found in the identification schemes, by indicating possible landscape-driven land cover mapping solutions to maximize classification performances.

Additional analysis on independent test areas and multi-scene acquisitions would contribute to fully define optimization strategies in the use of high dimensional remote sensing data and to strengthen the transferability of the proposed approach. However, the exploited remote sensing dataset and spatial domain are considered a good case study (in terms of multi-source imagery, size of the classification array, areal extension, and land cover variability) to quantify the multi-sensor capability for high resolution mapping of heterogeneous landscapes. In particular, the conducted analysis provided an experimental framework of the potential and limitations of the combined use of MIVIS, ADS40, and LiDAR sensors for classification tasks by focusing on certain natural- and human-dominated environments of interest for different application fields, such as urban planning, river restoration, agricultural, and forestry resource management. Future developments should focus on a better understanding of the contribution of ADS40 – that showed highly variable benefits across the tested feature space configurations – when used in combination with hyperspectral MIVIS and LiDAR data.

An advantage of airborne remote sensing, compared to satellite remote sensing, is the capability of offering very high spatial resolution images and detailed thematic maps. The main disadvantages are low coverage area and high cost per unit area of ground coverage. In light of the recent progresses in spaceborne sensor technology (e.g., ENMAP, Sentinel, ICESat/GLAS), the proposed approach can be viewed also as a preliminary investigation of the synergic use of spectral and laser data originating from different sources for fine-scale classification purposes, whose translation to forthcoming satellite systems would allow for higher cost-effectiveness of land use/land cover mapping, especially for continuous monitoring.

References

Anderson, J.E., Plourde, L.C., Martin, M.E., Braswell, B.H., Smith, M.L., Dubayah, R.O., Hofton, M.A., Blair, J.B., 2008. Integrating waveform lidar with hyperspectral imagery for inventory of a northern temperate forest. Remote Sensing of Environment 112, 1856–1870.

Belluco, E., Camuffo, M., Ferrari, S., Modenese, L., Silvestri, S., Marani, A., Marani, M., 2006. Mapping salt-marsh vegetation by multispectral and hyperspectral remote sensing. Remote Sensing of Environment 105 (1), 54–67.

Burrough, P.A., McDonell, R.A., 1998. Principles of Geographical Information Systems. Oxford University Press, NY, USA.

Cavalli, R.M., Fusilli, L., Pascucci, S., Pignatti, S., Santini, F., 2008. Hyperspectral sensor data capability for retrieving complex urban land cover in comparison with multispectral data: Venice city case study (Italy). Sensors 8, 3299–3320.

Chang, C.I., 2000. An information-theoretic approach to spectral variability, similarity, and discrimination for hyperspectral image analysis. IEEE Transactions on Information Theory 46, 1927–1932.

Chen, Y., Su, W., Li, J., Sun, Z., 2009. Hierarchical object oriented classification using very high resolution imagery and LIDAR data over urban areas. Advances in Space Research 43 (7), 1101–1110.

Claessens, L., Schoorl, J.M., Verburg, P.H., Geraedts, L., Veldkamp, A., 2009. Modelling interactions and feedback mechanisms between land use change and landscape processes. Agriculture Ecosystems & Environment 129 (1–3), 157–170.

Colombo, R., Meroni, M., Marchesi, A., Busetto, L., Rossini, M., Giardino, C., Panigada, C., 2008. Estimation of leaf and canopy water content in poplar plantations by means of hyperspectral indices and inverse modeling. Remote Sensing of Environment 112 (4), 1820–1834.

Dalponte, M., Bruzzone, L., Gianelle, D., 2008. Fusion of hyperspectral and lidar remote sensing data for classification of complex forest areas. IEEE Transactions on Geoscience and Remote Sensing 48 (5), 1416–1427.

de Jong, Y.M., van der Meer, F.D., 2004. Remote Sensing Image Analysis Including the Spatial Domain. Kluwer Academic Publishers, Dordrecht, Netherlands.

Duca, R., Del Frate, F., 2008. Hyperspectral and multiangle CHRIS–PROBA Images for the generation of land cover maps. IEEE Transactions on Geoscience and Remote Sensing 46 (10), 2857–2866.

Elaksher, A.F., 2008. Fusion of hyperspectral images and LiDAR-based dems for coastal mapping. Optical Laser Engineering 46 (7), 493–498.

Feddema, J.J., Oleson, K.W., Bonan, G.B., Mearns, L.O., Buja, L., Meehl, G., Washington, W.M., 2005. The importance of land cover change in simulating future climates. Science 310 (5754), 1674–1678.

Forzieri, G., Guarnieri, L., Vivoni, E.R., Castelli, F., Preti, F., 2009. Multiple attribute decision-making for individual tree detection using high-resolution laser scanning. Forest Ecology and Management 258 (11), 2501–2510.

Forzieri, G., Moser, G., Vivoni, E.R., Castelli, F., Canovaro, F., 2010. Riparian vegetation mapping for hydraulic roughness estimation using very high resolution remote sensing data fusion. Journal of Hydraulic Engineering. ASCE 136 (11), 855–867.

Forzieri, G., Catani, F., 2011. Scale-dependent relations in land cover biophysical dynamics. Ecological Modelling 222 (17), 3285–3290.

Forzieri, G., Moser, G., Catani, F. Assessment of hyperspectral MIVIS sensor capability for heterogeneous landscape classification. ISPRS Journal. Photogrammetry, http://dx.doi.org/10.1016/j.isprsjprs.2012.09.011, in press.

Forzieri, G., Castelli, F., Preti, F., 2012a. Advances in remote sensing of hydraulic roughness. International Journal of Remote Sensing 33 (2), 630–654.

Forzieri, G., Battistini, A., Catani, F., 2012b. ES4LUCC: a GIS-tool for remotely monitoring landscape dynamics. Computers & Geosciences 49, 72–80.

Gianinetto, M., Lechi, G., 2004. The development of superspectral approaches for the improvement of land cover classification. IEEE Transactions on Geoscience and Remote Sensing 42 (11), 2670–2679.

Goodenough, D.G., Dyk, A., Niemann, O., Pearlman, J.S., Chen, H., Han, T., Murdoch, M., West, C., 2003. Processing Hyperion and ALI for forest classification. IEEE Transactions on Geoscience and Remote Sensing 41 (6), 1321–1331.

Haralick, R.M., Shanmugan, K., Dinstein, I., 1973. Textural features for image classification. IEEE Transactions on Systems, Man and Cybernetics 3 (6), 610–621.

Hartigan, J.A., Hartigan, P.M., 1985. The dip test of unimodality. Annals of Statistics 13 (1), 70–84.

Herold, M., Liu, X., Clarke, K.C., 2003. Spatial metrics and image texture for mapping urban land use. Photogrammetric Engineering and Remote Sensing 69 (9), 991–1001.

Hirano, A., Madden, M., Welch, R., 2003. Hyperspectral image data for mapping wetland vegetation. Wetlands 23 (2), 436–448.

Hughes, G.F., 1968. On the mean accuracy of statistical pattern recognizers. IEEE Transactions on Information Theory 14 (1), 55–63.

Kottegoda, N.T., Rosso, R., 1997. Statistics, Probability, and Reliability for Civil and Environmental Engineers. McGraw-Hill, NY, USA.

Kruse, F.A., Lefkoff, A.B., Boardman, J.B., Heidebrecht, K.B., Shapiro, A.T., Barloon, P.J., Goetz, A.F.H., 1993. The spectral image processing system (SIPS)—interactive visualization and analysis of imaging spectrometer data. Remote Sensing of Environment 44 (2–3), 145–163.

Landgrebe, D., 2003. Signal Theory Methods in Multispectral Remote Sensing. John Wiley & Sons, Hoboken, NJ, USA.

Lillesand, T.M., Kiefer, R.W., Chipman, J.W., 2008. Remote Sensing and Image Interpretation, 6th ed. John Wiley & Sons, Hoboken, NJ, USA.

Lu, S., Oki, K., Shimizu, Y., Omasa, K., 2007. Comparison between several feature extraction/classification methods for mapping complicated agricultural land use patches using airborne hyperspectral data. International Journal of Remote Sensing 28 (5), 963–984.

Melesse, A.M., Weng, Q., Thenkabail, P.S., Senay, G.B., 2007. Remote sensing sensors and applications in environmental resources mapping and modelling. Sensors 7 (12), 3209–3241.

Melgani, F., Bruzzone, L., 2004. Classification of hyperspectral remote sensing images with support vector machines. IEEE Transactions on Geoscience and Remote Sensing 42 (8), 1778–1790.

Moser, G., Serpico, S.B. Combining support vector machines and Markov random fields in an integrated framework for contextual image classification. IEEE Transactions on Geoscience and Remote Sensing, http://dx.doi.org/10.1109/TGRS.2012.2211882, in press.

Moser, G., Serpico, S.B., Benediktsson, J.A. Land cover mapping by Markov modeling of spatial contextual information in very high resolution remote sensing images. Proceedings of the IEEE, http://dx.doi.org/10.1109/JPROC.2012.2211551, in press.

Mundt, J.T., Streutker, D.R., Glenn, N.F., 2006. Mapping sagebrush distribution using fusion of hyperspectral and lidar classifications. Photogrammetric Engineering and Remote Sensing 72, 47–54.

Navulur, K., 2007. Multispectral Image Analysis Using the Object-oriented Paradigm. CRC Press, Boca Raton, FL, USA.

Pignatti, S., Cavalli, R.M., Cuomo, V., Fusilli, L., Pascucci, S., Poscolieri, M., Santini, F., 2009. Evaluating Hyperion capability for land cover mapping in a fragmented eco system: Pollino National Park, Italy. Remote Sensing of Environment 113 (3), 622–634.

Pal, M., Mather, P.M., 2005. Support vector machines for classification in remote sensing. International Journal of Remote Sensing 26 (5), 1007–1011.

Priestnall, G., Jaafar, J., Duncan, A., 2000. Extracting urban features from LiDAR digital surface models. Computers Environment and Urban Systems 24 (2), 65–78.

Richards, J.A., Jia, X., 2006. Remote Sensing Digital Image Analysis, sixth ed. Springer-Verlag, Berlin, Germany.

Serpico, S.B., D'Incà, M., Melgani, F., Moser, G., 2002. A comparison of feature reduction techniques for classification of hyperspectral remote-sensing data. In: Proceedings of the SPIE—Conference on Image and Signal Processing for Remote Sensing VIII, Crete, Greece, September 22–27, 2002, pp. 347–358.

Serpico, S.B., Moser, G., 2007. Extraction of spectral channels from hyperspectral images for classification purposes. IEEE Transactions on Geoscience and Remote Sensing 45 (2), 484–495.

Spinetti, C., Mazzarini, F., Casacchia, R., Colini, L., Neri, M., Behncke, B., Salvatori, R., Buongiorno, M.F., Pareschi, M.T., 2009. Spectral properties of volcanic materials from hyperspectral field and satellite data compared with LiDAR data at Mt. Etna. The International Journal of Applied Earth Observation 11, 142–155.

Tansey, K., Chambers, I., Anstee, A., Denniss, A., Lamb, A., 2009. Object-oriented classification of very high resolution airborne imagery for the extraction cover in agricultural areas. Applied Geography 29 (2), 1145–1157.

Tso, B., Mather, P.M., 2000. Classification Methods for Remotely Sensed Data. CRC Press, Boca Raton, FL, USA.

van Der Meer, F.D., van Der Werff, H.M.A., van Ruitenbeek, F.J.A., Hecker, C.A., Bakker, W.H., Noomen, M.F., van Der Meijde, M., Carranza, E.J.M., Smeth, J.B.D., Woldai, T., 2012. Multi- and hyperspectral geologic remote sensing: a review. The International Journal of Applied Earth Observation 14, 112–128.

Wang, Z., Liu, S., Huang, X., 2010. Simulation of low-resolution panchromatic images by multivariate linear regression for pan-sharpening IKONOS imageries. IEEE Transactions on Geoscience and Remote Sensing 7 (3), 515–519.

Yuan, F., Sawaya, K.E., Loeffelholz, B.C., Bauer, M.E., 2005. Land cover classification and change analysis of the Twin Cities (Minnesota) Metropolitan Area by multitemporal Landsat remote sensing. Remote Sensing of Environment 98 (2–3), 317–328.

Zhang, B., Li, S., Jia, X., Gao, L., Peng, M., 2011. Adaptive Markov random field approach for classification of hyperspectral imagery. IEEE Transactions on Geoscience and Remote Sensing 8 (5), 972–977.